Title

Advanced MRI Techniques for the Ankle.

Journal

American Journal of Roentgenology, 209(3)

ISSN

0361-803X

Authors

Siriwanarangsun, Palanan
Bae, Won C
Statum, Sheronda
et al.

Publication Date

2017-09-01

DOI

10.2214/ajr.17.18057

Peer reviewed

HHS Public Access

Author manuscript

AJR Am J Roentgenol. Author manuscript; available in PMC 2021 June 12.

Published in final edited form as:

AJR Am J Roentgenol. 2017 September ; 209(3): 511–524. doi:10.2214/AJR.17.18057.

Advanced MRI Techniques for the Ankle

Palanan Siriwanarangsun, MD[3], **Won C. Bae, PhD**[1,2], **Sheronda Statum, MS, MBA**[1,2], **Christine B. Chung, MD**[1,2]

[1]Department of Radiology, VA San Diego Healthcare System, San Diego, CA [2]Department of Radiology, University of California-San Diego, La Jolla, CA [3]Department of radiology, Siriraj Hospital, Bangkok, Thailand

Abstract

Ankle injury is common in both the athletic and general population, with magnetic resonance imaging (MRI) the established non-invasive means of evaluation. This manuscript provides consideration for a state-of-the-art routine MR protocol of the ankle. It provides problem-solving tools based upon specific clinical indications. Further it introduces principles and implementation of novel Ultrashort Echo Time (UTE) MRI in the ankle, including morphologic and quantitative assessment.

Introduction

It is widely recognized that ankle injuries are common in the high performance athlete as well as the general population and account for up to 10% of emergency room visits [1–3]. Ankle injuries have been reported to represent the most common type of lesion in 24 of 70 sports, with ankle sprain being the most frequent [4]. Osteochondral lesions of the ankle are being recognized as an increasingly common injury, and have been reported in up to 50% of acute ankle injury, particularly those sports related [5–7]. Achilles tendon injury represents one of the most common sites of overuse injury in athletes, with pathology including the tendon and surrounding soft tissues [8].

Clearly, pathology that commonly affects the ankle varies in tissue type, mechanism of injury, and acute versus chronic presentation. When the complex anatomy of the ankle is factored into these components of the equation of MR diagnosis, it is necessary to leverage all tools at our disposal for accurate characterization of disease. The goal of this manuscript is to provide an update in MSK imaging techniques for ankle evaluation, targeting clinical questions or diagnostic challenges. It will offer guidance and considerations for routine protocol, indication driven protocols addressing specific clinical concerns, and finally profile the application of Ultrashort Echo Time (UTE) MR imaging techniques in the ankle.

Corresponding Author: Christine B. Chung, MD, [1]Department of Radiology, VA San Diego Healthcare System, 3350 La Jolla Village Dr., MC-114, San Diego, CA 92161, TEL: (619) 471-0514, FAX: (619) 471-0503, cbchung@ucsd.edu.

Disclosure: The authors declare that they have no conflict of interest

Routine Ankle Protocol

The acquisition of optimal MR images for the ankle has inherent challenges beyond its complex anatomy. The ankle represents the transition point between the distal lower leg and foot, those structures oriented at right angles to one another. Because of this relationship, imaging at or near the magic angle is difficult to avoid.

Its peripheral position obligates attention to maintain imaging at the isocenter of the bore to leverage homogeneous field strength and gradients. While consideration of imaging plane and pulse sequence choice will be primarily emphasized for both the routine protocol and tailored protocols, the coils for image acquisition cannot be taken for granted. It has been long since established that dedicated surface coils improve spatial resolution and field homogeneity, particularly for the imaging of small peripheral joints [9]. Dedicated extremity coils are generally implemented to optimize signal to noise [10]. The use of local transmit coils permits reduction in amount of radiofrequency (RF) power and associated specific absorption rate compared with receive-only coils. This allows for more slices per acquisition [11, 12]. The development of multichannel coils increases signal-to-noise-ratio (SNR) and the ability to use parallel imaging techniques [13].

While not crucial, there are significant advantages to ankle MR image acquisition on a 3T system. Clearly, the main advantage of higher field strength results from a near linear increase of SNR. The increase in SNR can be used to improve resolution, decrease scan time, or both. There are also potential drawbacks to increased field strength. Metallic susceptibility increases with increasing field strength, resulting in greater signal loss, geometric distortion and heterogeneous fat suppression, among other things. Chemical shift and pulsation artifacts are also more pronounced. T1, and to a lesser degree, T2 relaxation times are affected by field strength, requiring alterations in pulse sequence parameters [12].

The routine ankle MR protocol is practically based upon achieving a balance between spatial resolution and fluid sensitivity. The better spatial resolution yields better anatomical identification, and higher fluid sensitivity can improve overall detection of pathologic lesions. Non-contrast-enhanced fast spin-echo proton density-weighted or intermediate-weighted sequences are established as the anchor sequence for most protocols, and have been validated in the literature [10, 14, 15]. This corresponds to a long repetition time (>3500 milliseconds) and moderate echo time (28–34 milliseconds) [10]. The intermediate TE (between that of standard PD-weighted and T2-weighted sequences) offers a balance of SNR and fluid sensitivity. Without fat suppression, this sequence serves as an anatomic sequence with an arthrogram effect. It offers excellent contrast between fatty marrow and subchondral bone, subchondral bone and articular cartilage, as well articular cartilage and joint fluid. This sequence is broadly applied across joint to assess articular cartilage. It does not, however, unmask altered marrow signal in fatty tissues, and the sequence is susceptible to the magic angle effect. This is a phenomenon that accounts for signal changes in anisotropic tissues, such as articular cartilage or tendon [16, 17]. It occurs when collagen bundles are oriented 55 degrees to the main magnetic field, and mimics tendon degeneration. Non-fat suppressed intermediate- or proton density-weighted sequences can be replaced by T1-weighted sequences for anatomic evaluation, but do not have the added benefit of fluid

sensitivity. Inversion recovery sequences respond to both the need for a sequence that offers sensitivity to altered signal in fatty tissues, as well as one that is less susceptible to the magic angle effect [18, 19]. Table 1 provides a routine ankle MR protocol with imaging parameters and acquisition times noted.

Tailored Ankle Protocol – Indication Driven

It is quite common for MR imaging studies to be performed to address a specific clinical question. In the majority of cases, a routine MR protocol should accurately diagnose and characterize disease. There are, however, clinical or technical challenges that may benefit from implementation of additional tools in the MR armamentarium. From a clinical standpoint, patients often present in the subacute or chronic stage of disease where intrinsic tissue contrast does not allow facile diagnosis. Complex anatomy is certainly encountered in the foot and ankle with many curving structures. In addition, in some cases, the ability to render images in an alternative way can prove useful to referring physicians, offering them an interface that facilitates a better understanding of anatomic relationships, or extent of disease. Table 2 lists clinical and imaging conditions that may benefit from addition problem-solving imaging planes and sequences.

Specialized Imaging Planes

Several reports have introduced the concept of specialized imaging planes for evaluation of structures about the ankle. One such application includes the peroneal tendons, 2 of the 13 tendons that cross the ankle joint. Prior studies have reported variable accuracy in MRI diagnosis of peroneal pathology ranging from 56 to 100% [20, 21]. One pitfall in MR diagnosis of peroneal pathology certainly includes the interpretation of altered signal within these tendons, as they transition through a 90 degree directional change as they course from the ankle to their ultimate sights of attachment in the foot. Imaging the foot in 20 degrees of plantar flexion has been advocated to decrease magic angle effect [22–24]. In addition, an oblique sagittal plane, termed the “peroneal view” has been proposed for the evaluation of peroneal tendon pathology [25]. Peroneal views were acquired using 2 mm slice thickness in a plane parallel to a line between the lateral border of the posterior portion of the calcaneus and lateral margin of the peroneal tubercle at the mid-calcaneal level (Fig. 1B). This results in an image that profiles the peroneal tendons along their long axis, through their 90 degree directional change (Fig. 1C).

The value of oblique imaging planes has also been explored for evaluation of ankle ligaments. Injuries to the distal tibiofibular syndesmosis occurs in up to 11% of all ankle sprains, and may increase to more than 40% in contact or collision sports [26, 27]. The value of MRI in acute and chronic syndesmotic injuries has been described in several papers [27–29]. Since the anterior and posterior distal tibiofibular ligaments run obliquely to orthogonal planes, false-positive interpretation may result regarding the presence of a syndesmotic injury [28, 29] (Fig. 2A). Hermans, et al., proposed an oblique axial imaging plane (approximately 45 degrees) orthogonal to the course of the ligaments and concluded that it offered better interpretation of ligament continuity, thickening and contour [30] (Fig. 2B).

This technique has been adopted in MR ankle protocols and referred to as the “syndesmotic view” [31] (Fig. 2C).

Similarly, a tailored imaging plane has been described for evaluation of the calcaneofibular ligament. As with the syndesmotic ligaments, the calcaneofibular ligament runs oblique to conventional imaging planes. The angle formed by the ligament and calcaneal axis is about 13 degrees, and the angle of the ligament to the plantar fascia is about 55 degrees [32]. Routine MR has had low reported sensitivity and mediocre specificity and accuracy for the diagnosis of calcaneofibular ligament tears [33]. Park, et al., evaluated the utility of diagnostic accuracy of the oblique coronal plane (Fig. 3A) for visualization of the calcaneofibular ligament and diagnosis of injury. They concluded that it provided better anatomical evaluation and improved sensitivity and accuracy for diagnosis [33].

Inversion Recovery versus IV Contrast Administration

In general, the use of MRI with contrast material is not recommended by the American College of Radiology (ACR) in their consensus report of Appropriateness Criteria for acute trauma, chronic ankle pain, or stress fracture [34]. MRI with contrast is generally considered useful in the setting of suspected inflammatory arthritis, improving diagnostic accuracy in evaluation of synovitis and tenosynovitis, as well as serving as a way to evaluate response to therapy [35, 36]. Contrast enhanced MRI has also been shown to improve visibility of plantar plate lesions in the setting of metatarsalgia [37]. In an interesting article by Zubler, et al., the authors explored the additional value of T1-weighted contrast material-enhanced fat-suppressed MRI compared to STIR images in patients with acute and chronic pain. They hypothesized that the application of contrast would improve diagnostic accuracy, diagnostic confidence and correlation with pain. While their conclusions did not support contrast enhancement for routine MR protocols, they did document limited added value for soft tissue more than osseous lesions. Specifically, they illustrated a soft tissue lesion in the plantar fascia for which contrast enhancement markedly changed lesion grading.

Isotropic Three-Dimensional Fast Spin Echo Acquisition for Three-Dimensional Rendering

Isotropic three-dimensional fast spin echo volumetric acquisitions have emerged on all MR vendor platforms [38, 39]. These sequences have been leveraged in the literature to assess small anatomic structures due to their submillimeter, high-resolution source images [40–44]. Due to the isotropic, submillimeter nature of the acquisition and the approximation of tissue contrast that approaches 2D fast spin echo techniques, the possibility of scan once and reformat in any plane has become plausible [45, 46].

The value of 3D computed tomography (CT) reconstruction of osseous structures has been demonstrated in the literature for characterization of fracture, as well as guidance for hardware placement in the foot and ankle [47, 48]. CT has traditionally been the method used for evaluation of bone, 2D as well as 3D reconstructions. Studies are, however, emerging in the literature that show that MR provides resolution and contrast that allow equal or superior ability to detect osseous lesions compared with CT [49–51]. Recent studies have addressed the use of 3D MR sequences (Fig. 4A) to generate 3D renderings (Fig. 4B) of bone [51–53]. Radzi, et al., used 3D MRI to assess post-operative alignment in trauma

patients that sustained pilon fractures, and found performance comparable to 3D CT reconstructions [53]. Clearly, complex trauma, articular surface evaluation, and osseous alignment are among many potential indications in ankle evaluation that could benefit from 3D visualization. The capability to provide this information from MR imaging establishes a one-stop shop, where the patient can avoid the delay of an added imaging study [54]. Currently, off-line post-image processing is required to produce the 3D MR reconstructions. While various software packages can be used for this purpose, automated segmentation algorithms are not readily available.

MR Neurography

Many indications for detailed nerve evaluation exist in the ankle, including but not limited to tarsal tunnel syndrome, the diabetic foot, and entrapment syndromes [55–57]. MR evaluation of peripheral nerves requires a combination of sequences that provides high-resolution imaging and sensitivity to mobile water. Protocols based on a combination of T2 (Fig. 5A) and diffusion-weighted imaging (DWI) neurographic sequences predominate in the literature. These include T1 FSE, T2 adiabatic inversion recovery, proton density, 3D inversion recovery, and 3D diffusion-weighted reversed fast imaging with steady state precision (DW-PSIF) hybrid pulse sequences [58–61]. The DW-PSIF hybrid pulse sequence provides nerve-selective images (Fig. 5B), with suppression of adjacent vascular structures. The sequence can be implemented readily, but requires optimal shimming. Off isocenter imaging or large areas may be suffer from ghosting artifacts or poor fat suppression. Further, this sequence does require post-processing for image reformatting.

Metal artifact reduction sequences

Imaging around metal and in the postoperative setting provides significant challenges for MRI in the ankle [62]. The artifacts encountered are a result of differences in the magnetization between human tissue and metal prostheses [63, 64]. Four general types of artifact that can be seen include signal loss, signal pileup, geometric distortion, and failure of fat suppression. Basic MRI principles and consideration of magnetism, dephasing, and signal mis-registration, as well as the properties of the metal in question, promoted parameter changes in conventional MR sequences that are broadly referred to as Metal Artifact Reduction Sequences (MARS). Because magnetization and inhomogeneity are directly proportional to field strength, greater artifact is expected at 3 T than 1.5 T. Because susceptibility is inversely proportional to strength of the frequency encoding gradient, it is still possible to achieve reasonable metal artifact reduction with a 3-T MR scanner, though as a general rule, imaging at lower field strength is recommended [65]. Increasing matrix and decreasing slice thickness reduces intravoxel dephasing, but introduces the disadvantage of lower signal-to-noise ratio (SNR) [66]. This can be offset by increasing acquisition time, however, attention to ultimate scan time is required as patient motion will also degrade image quality. Perhaps most importantly, increasing receiver bandwidth will increase the strength of the frequency encoding gradient thereby reducing susceptibility. The use of spin-echo sequences corrects for dephasing caused by inhomogeneity (Fig. 6A and B). Gradient-echo sequences should be avoided. Shorter echo times result in less dephasing. Though inversion recovery sequences suffer from low SNR, they provide reasonable fat suppression as the fat profile depends on T1 recovery rather than precessional frequency [67] (Fig. 6C).

Metal artifact reduction sequences are now available on most vendor platforms, and include techniques such as view angle tilting (VAT), multiacquisition variable-resonance image correction (MAVRIC), and slice encoding metal artifact correction (SEMAC) [64, 68, 69]. VAT corrects for in-plane distortion by skewing readout data so the slice can be considered to be viewed at an angle. In this way, shifts in the slice-selection plane are correctly re-registered [70]. MAVRIC is a multispectral technique that improves both in-plane and through-plane artifact [71]. It decreases image artifacts (Fig. 7) by combining multiple individually acquired data sets at frequencies slightly offset from the dominant proton frequency. SEMAC also correct for in-plane and through-plane distortion. It applies additional phase encoding to correct through-plane distortion [66, 72]. MAVRIC and SEMAC have been found to reduce metal artifact with similar efficacy [73]. MAVRIC SL is a hybrid sequence that combines the additional phase encoding of SEMAC with spectral selectivity of MAVRIC to further minimize artifact [74]. A list of metallic reduction techniques and their availability are demonstrated in Table 3.

Novel Magnetic Resonance Pulse Sequence – Ultrashort Echo Time (UTE) MR Imaging

Rationale

There are many novel MR applications and works in progress (WIP's) that offer advantages in the realm of diagnosis and characterization of musculoskeletal pathology. UTE MRI, however, has introduced a paradigm shift in our understanding of the rather extreme limitations that conventional MR contrast mechanisms, conceived for brain evaluation with the advent of MR scanners, imposed upon a large cohort of musculoskeletal tissues. Conventional MR pulse sequences were originally applied and optimized for the longer T2 tissues of gray and white matter. All biological tissues, based upon their structure and composition, have individual intrinsic MR properties, among them the transverse relaxation time (T2 and T2*). The observed MRI signal intensity of a tissue depends upon many variables, including the mean transverse relaxation time. Tissues with short T2 relaxation times appear anechoic on conventional MR sequences. Logistically in these cases, after the excitation, the proton has relaxed before signal can be acquired. A commonly used classification scheme defines transverse relaxation values less than 0.1 ms as "supershort", 0.1 – 1 ms as "ultrashort", 1–10 ms as "short", and greater than 10 ms as long [75, 76]. The musculoskeletal tissues of bone, calcified layer of cartilage, tendon and ligament fall into the categories of short and ultrashort T2 tissues. As we consider the MR evaluation of these tissues with current grading schemes for pathology, it becomes readily apparent that we have limited capability to diagnose pathology in these tissues until they are transformed to long T2 tissues (i.e., severe disease in the form of fracture or tear), that can be characterized by standard MR contrast mechanisms.

Physics and Logistics

Given that UTE MRI techniques, largely WIP sequences that work on many modern 3T scanners without the necessity of hardware modification, should acquire signal from ultrashort and short T2 tissues, echo times less than 1 ms would be desirable. Standard MR

sequences cannot be used to generate echo times less than 1 ms on clinical MR scanners. The UTE sequence uses a short radiofrequency (RF) pulse and acquires data as soon as possible after excitation. Data acquisition occurs while the readout gradient is being ramped on. It uses a radial k-space sampling pattern that fills from the center out, and is nonlinear in time. 2D imaging slice selection is achieved with two excitations, each is a half conventional slice selection pulse using a positive and negative gradient that results in a single complete excitation pulse when combined. 3D imaging is achieved with a non-selective excitation pulse followed by a 3D radial acquisition [76]. Alternative approaches to pulse sequence construction result in variations of the UTE MRI, and include zero echo time (ZTE), sweep imaging with Fourier transformation (SWIFT), and pointwise encoding time reduction with radial acquisition (PETRA) [77–79].

With UTE MRI techniques, it is possible to obtain signal from tissues with short and ultrashort mean transverse relaxation times (Fig. 8A). It is important to realize that the acquisition of signal from short T2 tissues is only one component of unmasking its infrastructure. Several methods of fine tuning image contrast, such as echo subtraction to emphasize short T2 components (Fig. 8B), have been introduced in the literature and are beyond the scope of this manuscript. There is no question, however, that the application of UTE MRI techniques in the musculoskeletal system provide insight into the structural integrity of short T2 tissues in a way that we, as imagers, have never before encountered. Through this lens, the technique provides an opportunity to diagnose disease at a completely different point along the spectrum of severity.

Morphologic Assessment

In the ankle, the primary applications for UTE MRI techniques would include evaluation of the calcified layer of cartilage (Fig. 8) in the setting of talar dome injuries, tendon pathology, and entheseal pathology. Table 4 provided UTE imaging parameter that are used in our institute.

Calcified layer of cartilage—Ankle sprains have an estimated daily occurrence of 27,000 in the United States with 50% leading to osteochondral lesions [80, 81]. The osteochondral junction is comprised of hyaline articular cartilage, a deep zone of calcified cartilage that attaches the superficial cartilage to the subchondral bone. The region of calcified cartilage is quite thin and ranges in thickness from 79–239 microns [82]. Assessment of the calcified layer of cartilage is important in assessment of osteochondral injury, has been implicated in mechanisms for the development of osteoarthritis, and is important in the assessment of marrow-stimulating techniques for cartilage repair (abrasion, drilling, microfracture) [83]. In the latter, it is crucial to assess not only the presence and nature of fill tissue, but to verify the reconstitution of cartilage-bone interface [84–86].

Bae, et al., characterized the UTE MRI appearance of the calcified layer of cartilage as a linear region of increased signal intensity at the superficial cartilage – subchondral bone interface. In the setting of trauma, the calcified layer may be absent, whereas in degeneration, increasing thickness correlates with histologic descriptions [87].

Tendon/ Enthesis—The Achilles tendon (Fig. 9 and 10) is among the most frequently injured tendons of the body and can be the site of traumatic and overuse conditions as well as inflammatory conditions. Achilles tendinopathy is the most common cause of posterior heel pain, and is often caused by mechanical stress related to overload or overuse of the muscle-tendon unit [88]. Recent literature has implicated non-uniform mechanical loading of the triceps surae (lateral and medial gastrocnemius, soleus) with overuse conditions emphasizing a gap in our ability to non-invasively identify individual contributions and segmental structural changes in complex tendons [89]. In a broader sense, the entire spectrum of tensile tendon structural alteration that leads up to frank tearing and the short T2 tissue transformation to a pathologic long T2 tissue, is somewhat of a black box. Tissue characterization in microtrauma, degeneration, and repair with reference standards to tissue integrity and perhaps more importantly tissue function are highly desirable areas of development for UTE MRI techniques from the standpoint of clinical need [90, 91].

Similarly, the entheseal tendon has great interest from a clinical standpoint. The literature suggests that there is a significant cohort of seronegative patients with spondyloarthropathies who have subclinical disease involving the lower limb [92, 93] (Fig. 10).

Tendons are highly ordered structures with the tensile tendon structure dominated by type I collagen that is organized into fibrils and ultimately larger fiber bundle units (Fig. 9A). At the tendon attachment to bone, the enthesis or entheseal tendon, has a complex structural composition that functions to decrease mechanical stress from the soft tissue tensile tendon, to the osseous site of attachment. Robson, et al., demonstrated that UTE MRI was able to demonstrate the fascicular pattern of tensile tendon, as well as the complex structure of the entheseal tendon, or “entheseal organ”. In keeping with its mechanical function to serve as an intermediate between soft tissue and bone, the enthesis was demonstrated to have a fibrocartilaginous nodule within the tendon (analogous to a sesamoid bone) as well as at the interface to the bone [94]. UTE MRI demonstrates the regions of fibrocartilage with increased signal intensity, distinct from the fascicular appearance of the tensile tendon (Fig. 10A).

Quantitative Assessment

T2* mapping—UTE MRI techniques have also been applied for quantitative assessment of musculoskeletal tissues. MR-based techniques have been developed to allow characterization and quantification of the biochemical composition of tissue. This has been a crucial development for musculoskeletal MRI, allowing noninvasive assessment of biochemical, structural and possibly functional tissue status at early stages of disease, in repair tissue and the ability for longitudinal follow-up in all applications. The quantitative nature offers an objective data point.

In the ankle, the primary applications for quantitative evaluation include Achilles tendon (Figs. 9 and 10) and cartilage (Fig. 11). There is a growing body of literature that has established that T2* mapping is more sensitive to early structural changes in short T2 tissues than its long TE counterpart, standard T2 mapping. Both T2* and T2 relaxation data are acquired using a constant repetition time (TR) variable TE technique, in which signal intensities from regions of interest are plotted against TE (Fig. 9C), resulting in a map of T2

relaxation (Fig. 9B). The practical difference in the two techniques is the range of TE values used to create the map. In standard T2 mapping (Fig. 11A), the TE values range from 10 to 80 ms. In T2* mapping (Fig. 11B), the TE values range from less than 1 ms to 20 ms (Fig. 9B).

To date, clinical feasibility has been shown in evaluation of articular cartilage in the knee and hip, as well as Achilles tendon and the rotator cuff [95–99]. Quantitative T2* mapping of tendon(Figs. 9B and 10D). may be more complex than that of the calcified layer of cartilage. The latter is a tissue that is majority short T2 in nature with T2* values on the order of 1ms, whereas the tendon seems to have complex composition with significant variable T2* components, necessitating care in interpretation of quantitative data [90, 100]. In cadaveric tissue, a bicomponentT2* analysis showed short T2* fraction of normal appearing tendon was 79.2% with a mean T2* of 1.8 ms, with a long T2* fraction of 20.8% with a mean T2* of 2.5 ms [100].

Conclusion

Design of the ankle protocol remains stage-of-the-art depending on various trading off factors. Higher magnetic field improves SNR and reduce scan time although its increase metal artifact. Specialized imaging planes are useful in identifying and evaluating certain structures. However, prolong scanning time remains biggest draw back. MR neurography offers opportunity in evaluating small peripheral nerve with less interfering vascular signal. Metal reduction techniques should be applied in all cases that contain metal prosthesis. The MAVRIC and SEMAC have been found to reduce metal artifact with similar efficacy. Novel UTE sequence offers new contrast mechanism and clearly becoming valuable tool in both structural and quantitative evaluation.

References

1. Campbell SE, Warner M. MR imaging of ankle inversion injuries. Magn Reson Imaging Clin N Am 2008; 16:1–18, v [PubMed: 18440474]
2. Langner I, Frank M, Kuehn JP, et al. Acute inversion injury of the ankle without radiological abnormalities: assessment with high-field MR imaging and correlation of findings with clinical outcome. Skeletal radiology 2011; 40:423–430 [PubMed: 20706714]
3. Meehan TM, Martinez-Salazar EL, Torriani M. Aftermath of Ankle Inversion Injuries: Spectrum of MR Imaging Findings. Magn Reson Imaging Clin N Am 2017; 25:45–61 [PubMed: 27888851]
4. Fong DT, Hong Y, Chan LK, Yung PS, Chan KM. A systematic review on ankle injury and ankle sprain in sports. Sports Med 2007; 37:73–94 [PubMed: 17190537]
5. O'Loughlin PF, Heyworth BE, Kennedy JG. Current concepts in the diagnosis and treatment of osteochondral lesions of the ankle. Am J Sports Med 2010; 38:392–404 [PubMed: 19561175]
6. Saxena A, Eakin C. Articular talar injuries in athletes: results of microfracture and autogenous bone graft. Am J Sports Med 2007; 35:1680–1687 [PubMed: 17656737]
7. Schenck RC Jr., Goodnight JM. Osteochondritis dissecans. J Bone Joint Surg Am 1996; 78:439–456 [PubMed: 8613454]
8. Wong GN, Tan TJ. MR imaging as a problem solving tool in posterior ankle pain: A review. Eur J Radiol 2016; 85:2238–2256 [PubMed: 27842673]
9. Rivera M, Vaquero JJ, Santos A, Ruiz-Cabello J, del Pozo F. MRI visualization of small structures using improved surface coils. Magn Reson Imaging 1998; 16:157–166 [PubMed: 9508272]
10. Sofka CM. Technical Considerations: Best Practices for MR Imaging of the Foot and Ankle. Magn Reson Imaging Clin N Am 2017; 25:1–10 [PubMed: 27888842]

11. Collins MS, Felmlee JP. 3T magnetic resonance imaging of ankle and hindfoot tendon pathology. Top Magn Reson Imaging 2009; 20:175–188 [PubMed: 20410804]
12. Ramnath RR. 3T MR imaging of the musculoskeletal system (Part I): considerations, coils, and challenges. Magn Reson Imaging Clin N Am 2006; 14:27–40 [PubMed: 16530633]
13. Pruessmann KP. Parallel imaging at high field strength: synergies and joint potential. Top Magn Reson Imaging 2004; 15:237–244 [PubMed: 15548954]
14. Connell DA, Potter HG, Wickiewicz TL, Altchek DW, Warren RF. Noncontrast magnetic resonance imaging of superior labral lesions. 102 cases confirmed at arthroscopic surgery. Am J Sports Med 1999; 27:208–213 [PubMed: 10102103]
15. Mintz DN, Hooper T, Connell D, Buly R, Padgett DE, Potter HG. Magnetic resonance imaging of the hip: detection of labral and chondral abnormalities using noncontrast imaging. Arthroscopy 2005; 21:385–393 [PubMed: 15800516]
16. Bydder M, Rahal A, Fullerton GD, Bydder GM. The magic angle effect: a source of artifact, determinant of image contrast, and technique for imaging. J Magn Reson Imaging 2007; 25:290–300 [PubMed: 17260400]
17. Fullerton GD, Rahal A. Collagen structure: the molecular source of the tendon magic angle effect. J Magn Reson Imaging 2007; 25:345–361 [PubMed: 17260393]
18. Srikhum W, Nardo L, Karampinos DC, et al. Magnetic resonance imaging of ankle tendon pathology: benefits of additional axial short-tau inversion recovery imaging to reduce magic angle effects. Skeletal radiology 2013; 42:499–510 [PubMed: 23229628]
19. Othman MI, Chew KM, Peh WC. Variants and pitfalls in MR imaging of foot and ankle injuries. Semin Musculoskelet Radiol 2014; 18:54–62 [PubMed: 24515882]
20. Lamm BM, Myers DT, Dombek M, Mendicino RW, Catanzariti AR, Saltrick K. Magnetic resonance imaging and surgical correlation of peroneus brevis tears. J Foot Ankle Surg 2004; 43:30–36 [PubMed: 14752761]
21. O'Neil JT, Pedowitz DI, Kerbel YE, Codding JL, Zoga AC, Raikin SM. Peroneal Tendon Abnormalities on Routine Magnetic Resonance Imaging of the Foot and Ankle. Foot & ankle international 2016; 37:743–747 [PubMed: 26941162]
22. Gyftopoulos S, Bencardino JT. Normal variants and pitfalls in MR imaging of the ankle and foot. Magn Reson Imaging Clin N Am 2010; 18:691–705 [PubMed: 21111974]
23. Mengiardi B, Pfirrmann CW, Schottle PB, et al. Magic angle effect in MR imaging of ankle tendons: influence of foot positioning on prevalence and site in asymptomatic subjects and cadaveric tendons. European radiology 2006; 16:2197–2206 [PubMed: 16568266]
24. Taljanovic MS, Alcala JN, Gimber LH, Rieke JD, Chilvers MM, Latt LD. High-resolution US and MR imaging of peroneal tendon injuries--erratum. Radiographics : a review publication of the Radiological Society of North America, Inc 2015; 35:651
25. Park HJ, Lee SY, Kim E, et al. Peroneal tendon pathology evaluation using the oblique sagittal plane in ankle MR imaging. Acta Radiol 2016; 57:620–626 [PubMed: 26253929]
26. Gerber JP, Williams GN, Scoville CR, Arciero RA, Taylor DC. Persistent disability associated with ankle sprains: a prospective examination of an athletic population. Foot & ankle international 1998; 19:653–660 [PubMed: 9801078]
27. Hopkinson WJ, St Pierre P, Ryan JB, Wheeler JH. Syndesmosis sprains of the ankle. Foot Ankle 1990; 10:325–330 [PubMed: 2113510]
28. Oae K, Takao M, Naito K, et al. Injury of the tibiofibular syndesmosis: value of MR imaging for diagnosis. Radiology 2003; 227:155–161 [PubMed: 12616009]
29. Takao M, Ochi M, Oae K, Naito K, Uchio Y. Diagnosis of a tear of the tibiofibular syndesmosis. The role of arthroscopy of the ankle. J Bone Joint Surg Br 2003; 85:324–329 [PubMed: 12729102]
30. Hermans JJ, Ginai AZ, Wentink N, Hop WC, Beumer A. The additional value of an oblique image plane for MRI of the anterior and posterior distal tibiofibular syndesmosis. Skeletal radiology 2011; 40:75–83 [PubMed: 20549205]
31. Chun KY, Choi YS, Lee SH, et al. Deltoid Ligament and Tibiofibular Syndesmosis Injury in Chronic Lateral Ankle Instability: Magnetic Resonance Imaging Evaluation at 3T and Comparison with Arthroscopy. Korean J Radiol 2015; 16:1096–1103 [PubMed: 26356649]

32. Boonthathip M, Chen L, Trudell D, Resnick D. Lateral ankle ligaments: MR arthrography with anatomic correlation in cadavers. Clin Imaging 2011; 35:42–48 [PubMed: 21237417]
33. Park HJ, Lee SY, Park NH, et al. Usefulness of the oblique coronal plane in ankle MRI of the calcaneofibular ligament. Clinical radiology 2015; 70:416–423 [PubMed: 25573813]
34. Bancroft LW, Kransdorf MJ, Adler R, et al. ACR Appropriateness Criteria Acute Trauma to the Foot. J Am Coll Radiol 2015; 12:575–581 [PubMed: 25935824]
35. Stomp W, Krabben A, van der Heijde D, et al. Aiming for a simpler early arthritis MRI protocol: can Gd contrast administration be eliminated? European radiology 2015; 25:1520–1527 [PubMed: 25636414]
36. Sudol-Szopinska I, Jurik AG, Eshed I, et al. Recommendations of the ESSR Arthritis Subcommittee for the Use of Magnetic Resonance Imaging in Musculoskeletal Rheumatic Diseases. Semin Musculoskelet Radiol 2015; 19:396–411 [PubMed: 26583367]
37. Dinoa V, von Ranke F, Costa F, Marchiori E. Evaluation of lesser metatarsophalangeal joint plantar plate tears with contrast-enhanced and fat-suppressed MRI. Skeletal radiology 2016; 45:635–644 [PubMed: 26887801]
38. Gold GE, Busse RF, Beehler C, et al. Isotropic MRI of the knee with 3D fast spin-echo extended echo-train acquisition (XETA): initial experience. AJR American journal of roentgenology 2007; 188:1287–1293 [PubMed: 17449772]
39. Notohamiprodjo M, Horng A, Pietschmann MF, et al. MRI of the knee at 3T: first clinical results with an isotropic PDfs-weighted 3D-TSE-sequence. Investigative radiology 2009; 44:585–597 [PubMed: 19668001]
40. Park HJ, Lee SY, Choi SH, et al. Comparison of oblique coronal images in knee of three-dimensional isotropic T2-weighted turbo spin echo MRI versus two-dimensional fast spin echo T2-weighted sequences for evaluation of posterior cruciate ligament injury. Br J Radiol 2016; 89:20160554 [PubMed: 27653673]
41. Park HJ, Lee SY, Choi YJ, et al. 3D isotropic T2-weighted fast spin echo (VISTA) versus 2D T2-weighted fast spin echo in evaluation of the calcaneofibular ligament in the oblique coronal plane. Clinical radiology 2017; 72:176 e171–176 e177
42. Park HJ, Lee SY, Park NH, et al. Three-dimensional isotropic T2-weighted fast spin-echo (VISTA) knee MRI at 3.0 T in the evaluation of the anterior cruciate ligament injury with additional views: comparison with two-dimensional fast spin-echo T2-weighted sequences. Acta Radiol 2016; 57:1372–1379 [PubMed: 25585852]
43. Park HJ, Lee SY, Park NH, et al. Three-dimensional isotropic T2-weighted fast spin-echo (VISTA) ankle MRI versus two-dimensional fast spin-echo T2-weighted sequences for the evaluation of anterior talofibular ligament injury. Clinical radiology 2016; 71:349–355 [PubMed: 26774370]
44. Yi J, Cha JG, Lee YK, Lee BR, Jeon CH. MRI of the anterior talofibular ligament, talar cartilage and os subfibulare: Comparison of isotropic resolution 3D and conventional 2D T2-weighted fast spin-echo sequences at 3.0 T. Skeletal radiology 2016; 45:899–908 [PubMed: 26992909]
45. Kijowski R, Davis KW, Woods MA, et al. Knee joint: comprehensive assessment with 3D isotropic resolution fast spin-echo MR imaging--diagnostic performance compared with that of conventional MR imaging at 3.0 T. Radiology 2009; 252:486–495 [PubMed: 19703886]
46. Rosas H, Kijowski R. Volumetric magnetic resonance imaging of the musculoskeletal system. Semin Roentgenol 2013; 48:140–147 [PubMed: 23452461]
47. Qiang M, Chen Y, Zhang K, Li H, Dai H. Effect of sustentaculum screw placement on outcomes of intra-articular calcaneal fracture osteosynthesis: A prospective cohort study using 3D CT. Int J Surg 2015; 19:72–77 [PubMed: 25980397]
48. Roll C, Schirmbeck J, Muller F, Neumann C, Kinner B. Value of 3D Reconstructions of CT Scans for Calcaneal Fracture Assessment. Foot & ankle international 2016; 37:1211–1217 [PubMed: 27530985]
49. Collin D, Geijer M, Gothlin JH. Computed tomography compared to magnetic resonance imaging in occult or suspect hip fractures. A retrospective study in 44 patients. European radiology 2016; 26:3932–3938 [PubMed: 26747255]

50. Gyftopoulos S, Hasan S, Bencardino J, et al. Diagnostic accuracy of MRI in the measurement of glenoid bone loss. AJR American journal of roentgenology 2012; 199:873–878 [PubMed: 22997381]
51. Gyftopoulos S, Yemin A, Mulholland T, et al. 3DMR osseous reconstructions of the shoulder using a gradient-echo based two-point Dixon reconstruction: a feasibility study. Skeletal radiology 2013; 42:347–352 [PubMed: 22829026]
52. Glaser C, D'Anastasi M, Theisen D, et al. Understanding 3D TSE Sequences: Advantages, Disadvantages, and Application in MSK Imaging. Semin Musculoskelet Radiol 2015; 19:321–327 [PubMed: 26583360]
53. Radzi S, Dlaska CE, Cowin G, et al. Can MRI accurately detect pilon articular malreduction? A quantitative comparison between CT and 3T MRI bone models. Quant Imaging Med Surg 2016; 6:634–647 [PubMed: 28090442]
54. Bae WC, Ruangchaijatuporn T, Chung CB. New Techniques in MR Imaging of the Ankle and Foot. Magn Reson Imaging Clin N Am 2017; 25:211–225 [PubMed: 27888849]
55. Burge AJ, Gold SL, Kuong S, Potter HG. High-resolution magnetic resonance imaging of the lower extremity nerves. Neuroimaging Clin N Am 2014; 24:151–170 [PubMed: 24210318]
56. Chhabra A, Subhawong TK, Williams EH, et al. High-resolution MR neurography: evaluation before repeat tarsal tunnel surgery. AJR American journal of roentgenology 2011; 197:175–183 [PubMed: 21701028]
57. Pham M, Oikonomou D, Hornung B, et al. Magnetic resonance neurography detects diabetic neuropathy early and with Proximal Predominance. Ann Neurol 2015; 78:939–948 [PubMed: 26381658]
58. Chhabra A, Subhawong TK, Carrino JA. MR imaging of deltoid ligament pathologic findings and associated impingement syndromes. Radiographics : a review publication of the Radiological Society of North America, Inc 2010; 30:751–761
59. Chhabra A Peripheral MR neurography: approach to interpretation. Neuroimaging Clin N Am 2014; 24:79–89 [PubMed: 24210314]
60. Chhabra A, Belzberg AJ, Rosson GD, et al. Impact of high resolution 3 tesla MR neurography (MRN) on diagnostic thinking and therapeutic patient management. European radiology 2016; 26:1235–1244 [PubMed: 26396110]
61. Chhabra A, Soldatos T, Subhawong TK, et al. The application of three-dimensional diffusion-weighted PSIF technique in peripheral nerve imaging of the distal extremities. J Magn Reson Imaging 2011; 34:962–967 [PubMed: 21769979]
62. LiMarzi GM, Scherer KF, Richardson ML, et al. CT and MR Imaging of the Postoperative Ankle and Foot. Radiographics : a review publication of the Radiological Society of North America, Inc 2016; 36:1828–1848
63. Hargreaves BA, Worters PW, Pauly KB, Pauly JM, Koch KM, Gold GE. Metal-induced artifacts in MRI. AJR American journal of roentgenology 2011; 197:547–555 [PubMed: 21862795]
64. Toms AP, Smith-Bateman C, Malcolm PN, Cahir J, Graves M. Optimization of metal artefact reduction (MAR) sequences for MRI of total hip prostheses. Clinical radiology 2010; 65:447–452 [PubMed: 20451011]
65. Liebl H, Heilmeier U, Lee S, et al. In vitro assessment of knee MRI in the presence of metal implants comparing MAVRIC-SL and conventional fast spin echo sequences at 1.5 and 3 T field strength. J Magn Reson Imaging 2015; 41:1291–1299 [PubMed: 24912802]
66. Lu W, Pauly KB, Gold GE, Pauly JM, Hargreaves BA. SEMAC: Slice Encoding for Metal Artifact Correction in MRI. Magn Reson Med 2009; 62:66–76 [PubMed: 19267347]
67. Ariyanayagam T, Malcolm PN, Toms AP. Advances in Metal Artifact Reduction Techniques for Periprosthetic Soft Tissue Imaging. Semin Musculoskelet Radiol 2015; 19:328–334 [PubMed: 26583361]
68. Chang EY, Bae WC, Chung CB. Imaging the knee in the setting of metal hardware. Magn Reson Imaging Clin N Am 2014; 22:765–786 [PubMed: 25442032]
69. Sofka CM. Postoperative magnetic resonance imaging of the foot and ankle. J Magn Reson Imaging 2013; 37:556–565 [PubMed: 23423796]

70. Cho ZH, Kim DJ, Kim YK. Total inhomogeneity correction including chemical shifts and susceptibility by view angle tilting. Med Phys 1988; 15:7–11 [PubMed: 3352554]
71. Koch KM, Lorbiecki JE, Hinks RS, King KF. A multispectral three-dimensional acquisition technique for imaging near metal implants. Magn Reson Med 2009; 61:381–390 [PubMed: 19165901]
72. Lu W, Pauly KB, Gold GE, Pauly JM, Hargreaves BA. Slice encoding for metal artifact correction with noise reduction. Magn Reson Med 2011; 65:1352–1357 [PubMed: 21287596]
73. Chen CA, Chen W, Goodman SB, et al. New MR imaging methods for metallic implants in the knee: artifact correction and clinical impact. J Magn Reson Imaging 2011; 33:1121–1127 [PubMed: 21509870]
74. Koch KM, Brau AC, Chen W, et al. Imaging near metal with a MAVRIC-SEMAC hybrid. Magn Reson Med 2011; 65:71–82 [PubMed: 20981709]
75. Bydder GM. Review. The Agfa Mayneord lecture: MRI of short and ultrashort T(2) and T(2)* components of tissues, fluids and materials using clinical systems. Br J Radiol 2011; 84:1067–1082 [PubMed: 22101579]
76. Chang EY, Du J, Chung CB. UTE imaging in the musculoskeletal system. J Magn Reson Imaging 2015; 41:870–883 [PubMed: 25045018]
77. Zhang J, Idiyatullin D, Corum CA, Kobayashi N, Garwood M. Gradient-modulated SWIFT. Magn Reson Med 2016; 75:537–546 [PubMed: 25800547]
78. Grodzki DM, Jakob PM, Heismann B. Ultrashort echo time imaging using pointwise encoding time reduction with radial acquisition (PETRA). Magn Reson Med 2012; 67:510–518 [PubMed: 21721039]
79. Weiger M, Brunner DO, Dietrich BE, Muller CF, Pruessmann KP. ZTE imaging in humans. Magn Reson Med 2013; 70:328–332 [PubMed: 23776142]
80. Savage-Elliott I, Ross KA, Smyth NA, Murawski CD, Kennedy JG. Osteochondral lesions of the talus: a current concepts review and evidence-based treatment paradigm. Foot Ankle Spec 2014; 7:414–422 [PubMed: 25100765]
81. Bae WC, Dwek JR, Znamirowski R, et al. Ultrashort echo time MR imaging of osteochondral junction of the knee at 3 T: identification of anatomic structures contributing to signal intensity. Radiology 2010; 254:837–845 [PubMed: 20177096]
82. Lane LB, Bullough PG. Age-related changes in the thickness of the calcified zone and the number of tidemarks in adult human articular cartilage. J Bone Joint Surg Br 1980; 62:372–375 [PubMed: 7410471]
83. Thambyah A, Broom N. On how degeneration influences load-bearing in the cartilage-bone system: a microstructural and micromechanical study. Osteoarthritis Cartilage 2007; 15:1410–1423 [PubMed: 17689989]
84. Chen H, Chevrier A, Hoemann CD, Sun J, Ouyang W, Buschmann MD. Characterization of subchondral bone repair for marrow-stimulated chondral defects and its relationship to articular cartilage resurfacing. Am J Sports Med 2011; 39:1731–1740 [PubMed: 21628638]
85. Domayer SE, Apprich S, Stelzeneder D, et al. Cartilage repair of the ankle: first results of T2 mapping at 7.0 T after microfracture and matrix associated autologous cartilage transplantation. Osteoarthritis Cartilage 2012; 20:829–836 [PubMed: 22542632]
86. Domayer SE, Welsch GH, Stelzeneder D, et al. Microfracture in the Ankle: Clinical Results and MRI with T2-Mapping at 3.0 T after 1 to 8 Years. Cartilage 2011; 2:73–80 [PubMed: 26069571]
87. Hargrave-Thomas E, van Sloun F, Dickinson M, Broom N, Thambyah A. Multi-scalar mechanical testing of the calcified cartilage and subchondral bone comparing healthy vs early degenerative states. Osteoarthritis Cartilage 2015; 23:1755–1762 [PubMed: 26028136]
88. Berner J, Zufferey P. [Achilles tendinopathy]. Rev Med Suisse 2015; 11:606–608, 610–601 [PubMed: 25946872]
89. Toumi H, Larguech G, Cherief M, et al. Implications of the calf musculature and Achilles tendon architectures for understanding the site of injury. J Biomech 2016; 49:1180–1185 [PubMed: 26994783]

90. Chang EY, Du J, Iwasaki K, et al. Single- and Bi-component T2* analysis of tendon before and during tensile loading, using UTE sequences. J Magn Reson Imaging 2015; 42:114–120 [PubMed: 25223714]
91. Koff MF, Pownder SL, Shah PH, Yang LW, Potter HG. Ultrashort echo imaging of cyclically loaded rabbit patellar tendon. J Biomech 2014; 47:3428–3432 [PubMed: 25234349]
92. Bandinelli F, Milla M, Genise S, et al. Ultrasound discloses entheseal involvement in inactive and low active inflammatory bowel disease without clinical signs and symptoms of spondyloarthropathy. Rheumatology (Oxford) 2011; 50:1275–1279 [PubMed: 21317135]
93. Bandinelli F, Prignano F, Bonciani D, et al. Ultrasound detects occult entheseal involvement in early psoriatic arthritis independently of clinical features and psoriasis severity. Clin Exp Rheumatol 2013; 31:219–224 [PubMed: 23190740]
94. Robson MD, Benjamin M, Gishen P, Bydder GM. Magnetic resonance imaging of the Achilles tendon using ultrashort TE (UTE) pulse sequences. Clinical radiology 2004; 59:727–735 [PubMed: 15262548]
95. Sneag DB, Shah P, Koff MF, Lim WY, Rodeo SA, Potter HG. Quantitative Ultrashort Echo Time Magnetic Resonance Imaging Evaluation of Postoperative Menisci: a Pilot Study. HSS J 2015; 11:123–129 [PubMed: 26140031]
96. Williams A, Qian Y, Chu CR. UTE-T2 * mapping of human articular cartilage in vivo: a repeatability assessment. Osteoarthritis Cartilage 2011; 19:84–88 [PubMed: 21035556]
97. Williams A, Qian Y, Golla S, Chu CR. UTE-T2 * mapping detects sub-clinical meniscus injury after anterior cruciate ligament tear. Osteoarthritis Cartilage 2012; 20:486–494 [PubMed: 22306000]
98. Krepkin K, Bruno M, Raya JG, Adler RS, Gyftopoulos S. Quantitative assessment of the supraspinatus tendon on MRI using T2/T2* mapping and shear-wave ultrasound elastography: a pilot study. Skeletal radiology 2017; 46:191–199 [PubMed: 27896400]
99. Gardin A, Rasinski P, Berglund J, Shalabi A, Schulte H, Brismar TB. T2 * relaxation time in Achilles tendinosis and controls and its correlation with clinical score. J Magn Reson Imaging 2016; 43:1417–1422 [PubMed: 26605756]
100. Chang EY, Du J, Statum S, Pauli C, Chung CB. Quantitative bi-component T2* analysis of histologically normal Achilles tendons. Muscles Ligaments Tendons J 2015; 5:58–62 [PubMed: 26261782]

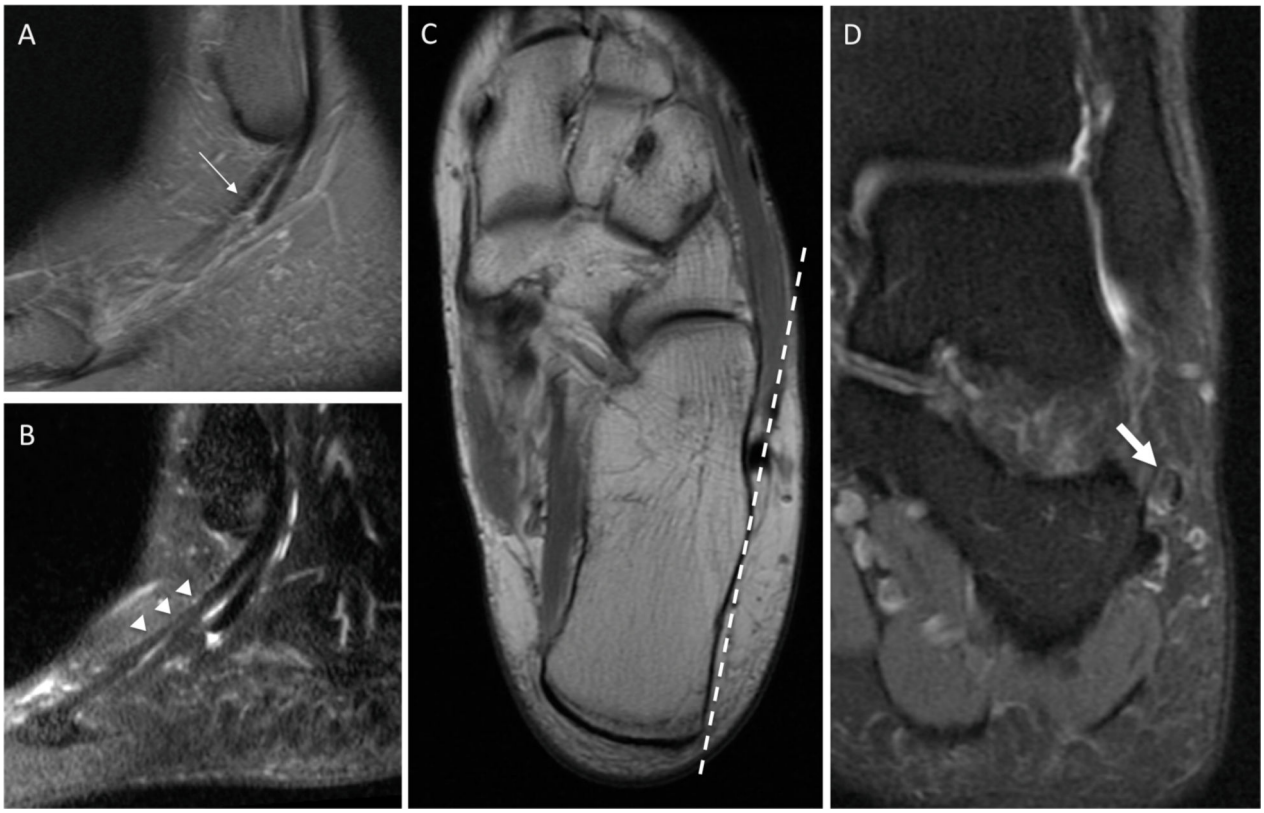

Fig. 1–.

A 37-year male with split tear of peroneus brevis tendon.

A, T2-weight (T2w) sagittal image (TR/TE 2750/66 ms) with fat saturation. Slight high signal of the peroneus brevis tendon (thick arrow) and partially seen the distal portion[**A**]. **B** and **C**, T2w fat saturation image in sagittal oblique peroneal planes [**B**] and axial proton density weight image [**C**] (TR/TE 2000/76 ms, 2075/43 ms). The sagittal oblique peroneal planes [**B**] generate by tilting the sagittal image in oblique orientation (the dash line in axial image [**C**]), High signal at distal portion of the peroneus brevis tendon (arrow heads) with central linear fluid signal indicating split tear.

D, Proton density-weighted fat suppressed image in coronal plane (TR/TE 2925/26.3) confirms the finding of split tear peroneus brevis seen on sagittal oblique peroneal plane [**B**].

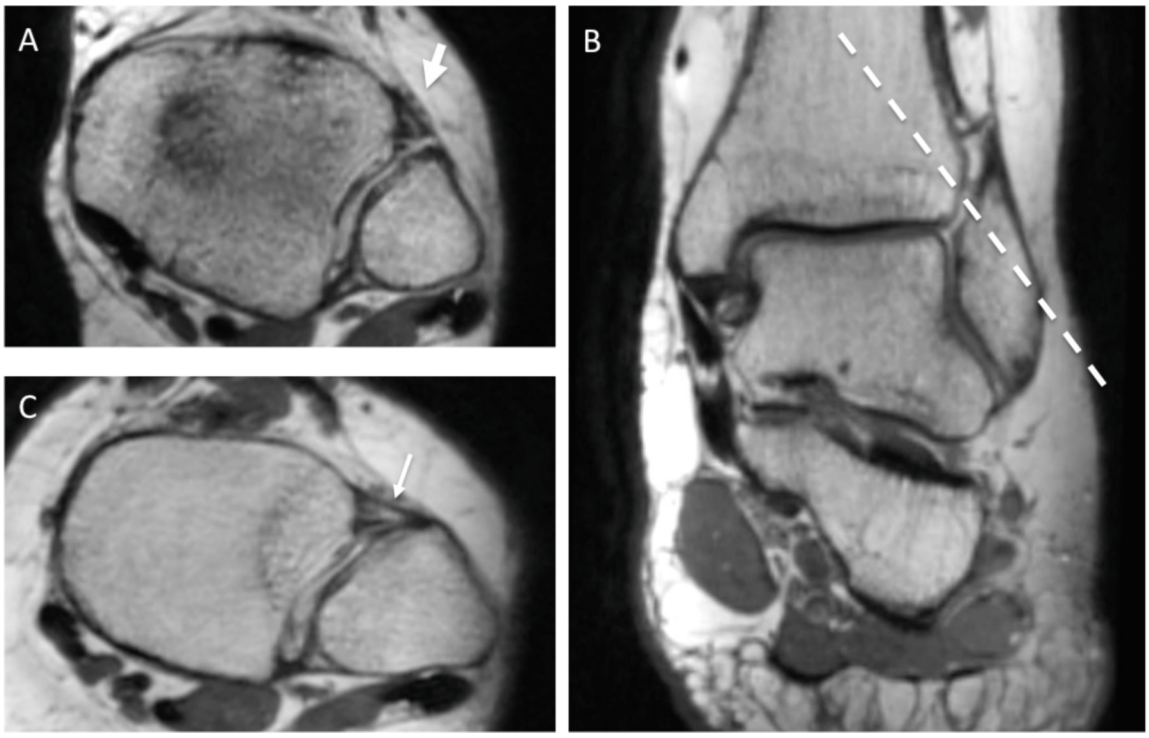

Fig. 2–.

Proton density-weight images of the ankle (TR/TE, 2000/37 ms) in different imaging planes. **A**, In the axial plane, the tibiofibular ligament (thick arrow) is only partially visible due to marked oblique orientation of the ligament.

B and **C**, In coronal [**B**] and oblique syndesmosis [**C**] planes generate by tilting the axial image in oblique orientation (the dash line in coronal image [**B**]), a normal continuation of the anterior tibiofibular ligament (thin arrow) can be appreciated.

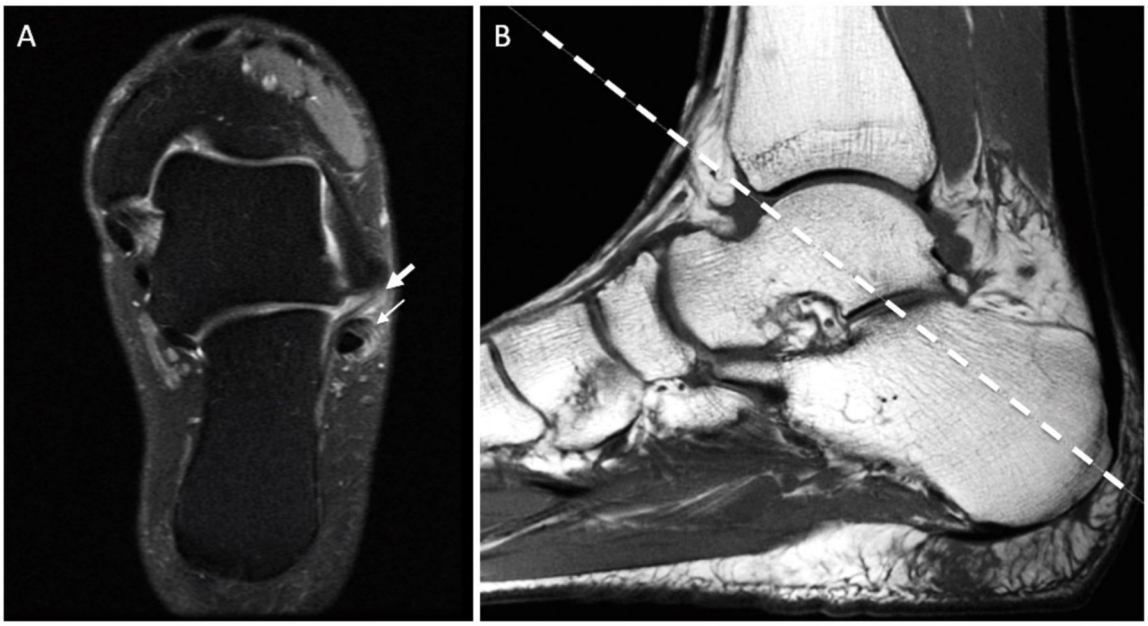

Fig. 3–.

A 35-year-old male with split tear of the peroneus brevis tendon.

A and **B**, Proton density-weighted (PDw) image with fat saturation in Calcaneofibular ligament plane [**A**] (seen as dash line in the sagittal PDw image [**B**]). (TR/TE, 2925/26 ms [**A**] and 3225/34 ms [**B**]) Note increase signal intensity and separation of the peroneus brevis tendon was observed (thin arrow, **A**). High signal intensity and thickening of the adjacent calcaneofibular ligament was also depicted (thick arrow, **A**).

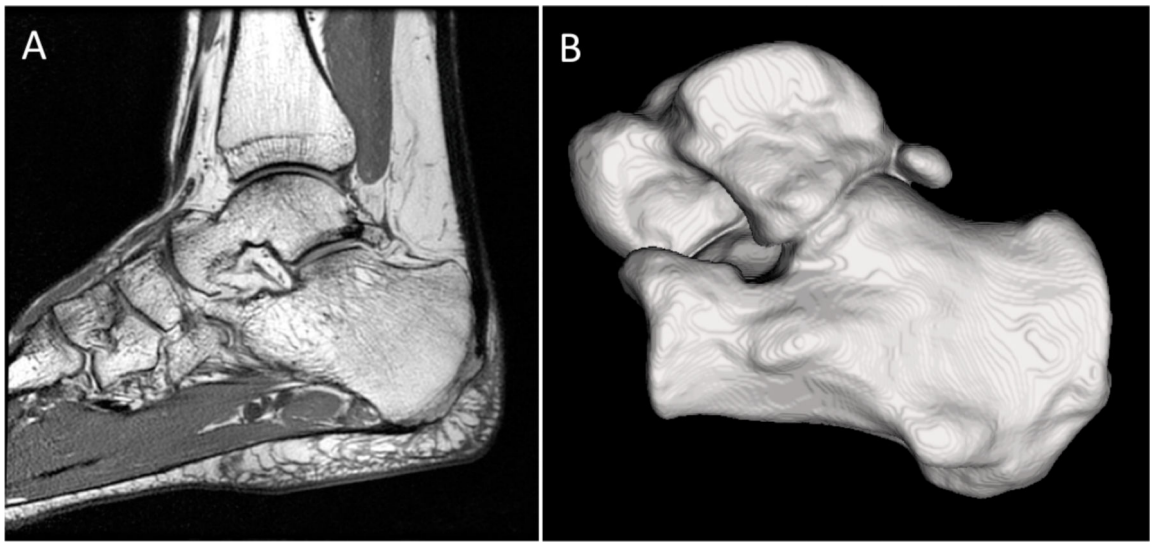

Fig. 4–.

3D volume rendering of the talus and calcaneus.

A, Sagittal high-resolution Isotropic three-dimensional fast spin echo volumetric acquisition image of the ankle obtained at submillimeter (0.4 mm) isotropic resolution (TR/TE, 800/19 ms).

B, 3D volume rendering of the talus and calcaneus in lateral view.

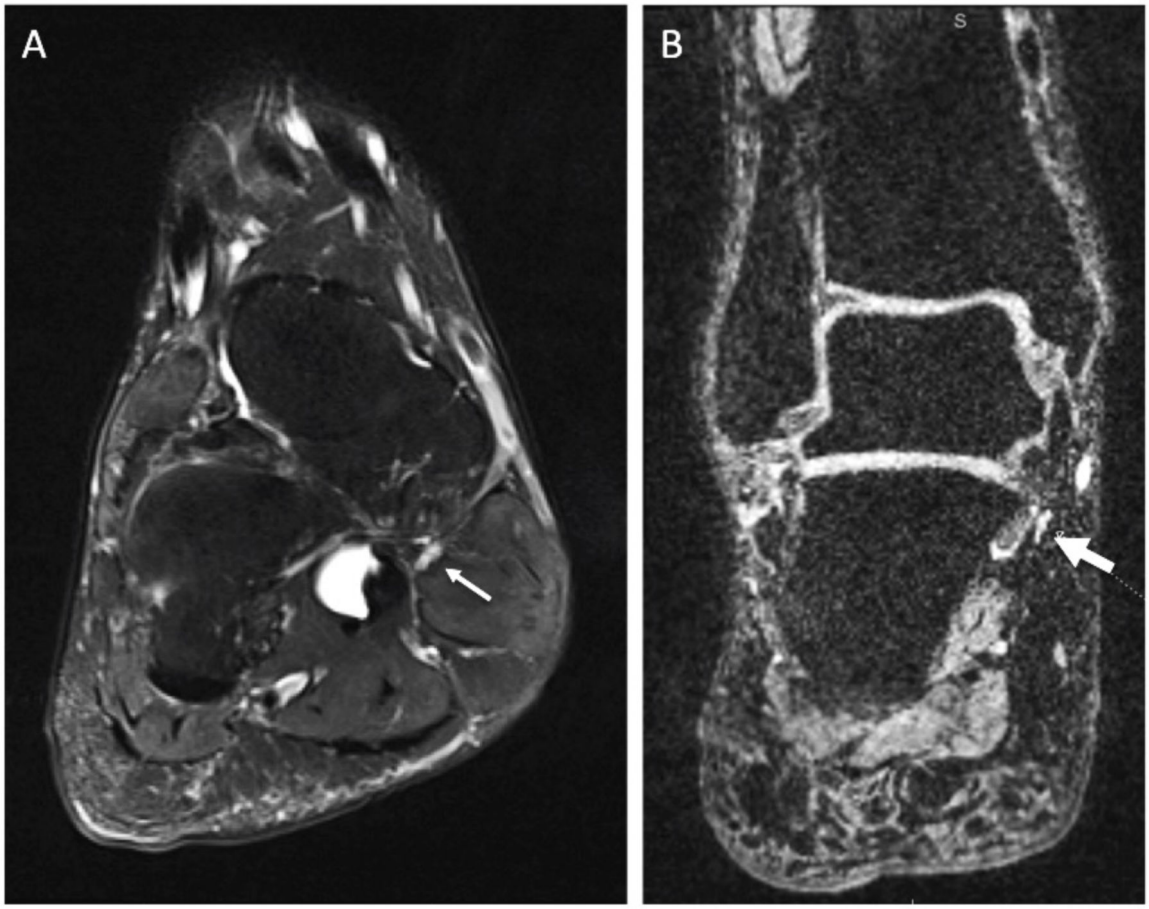

Fig. 5–.

Ankle MR neurography of a 49-year-old male presented with shooting pain along plantar medial aspect of the mid foot.

A, Coronal T2-weighted image with fat saturation revealed fluid surrounding the flexor hallucis longus tendon suggesting tenosynovitis. Increased signal intensity and thickening of the adjacent medial plantar nerve (thin arrow) were found.

B, 3D Diffusion-weighted reversed fast imaging with steady state precision (DW-PSIF) image showed hypersignal intensity of the medial plantar nerve at level of Henry's knot (thick arrow). (*Courtesy of Dr. Jenny T. Bencardino, M.D., Professor of Radiology and Orthopaedic Surgery NYU School of Medicine, New York, NY*)

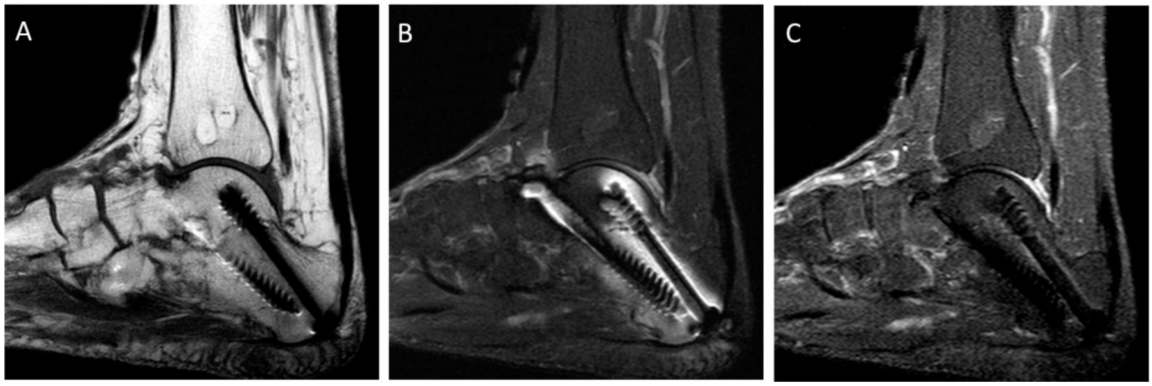

Fig. 6–.

74-year-old female with status post triple arthrodesis.

A, **B** and **C**, Sagittal image FSE PDw [**A**], FSE T2w with fat saturation [**B**] and Short Tau Inversion Recovery (STIR) [**C**] (TR/TE 580/20 [A], 2010/42 [**B**], 2156/25 [**C**]) in 1.5 T scanner. Increase metallic pile up and in plane artifacts during fat saturation sequence [**B**] as compared to non fat saturation sequence [**A**]. Adequate fat saturation without increase in artifact on STIR [**C**] was observed. (*Courtesy of Dr. Laura Bancroft, M.D., Professor of Radiology, Florida Hospital Orlando, University of Central Florida College of Medicine, Orlando, FL*)

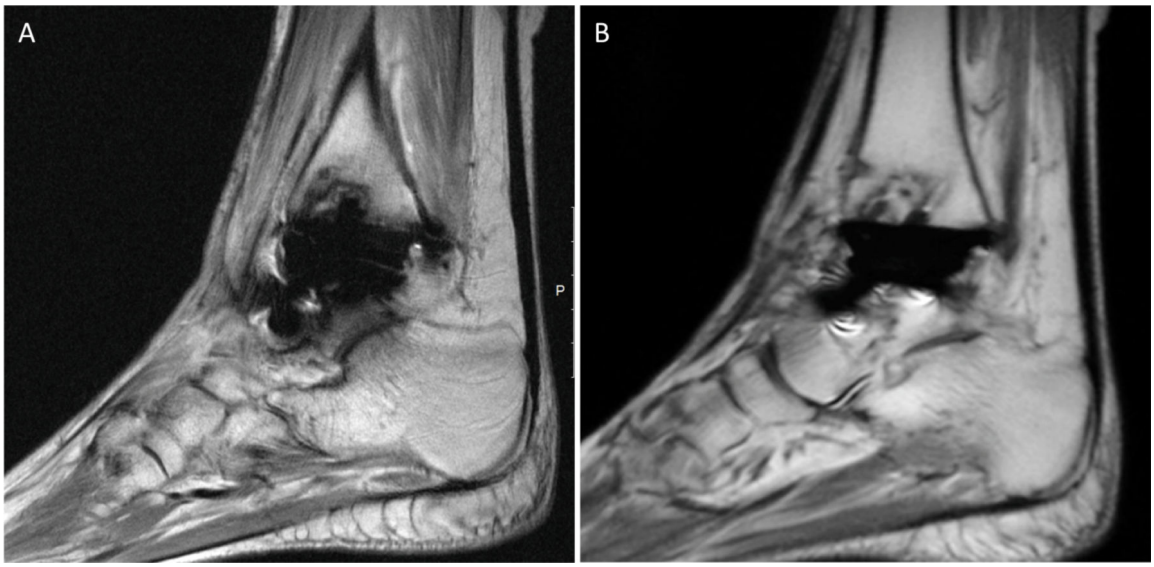

Fig. 7 –.

Demonstration of ankle imaging in the presence of total ankle arthroplasty in a 52-year-old female with demonstrate placement of total ankle arthroplasty. Additional medial malleolar buttress screw as well as syndesmotic fusion utilizing tightrope technique were performed. **A** and **B**, Sagittal proton density-weighted (PDw) images using fast spin echo [**A**] and MAVRIC [**B**] (TR/TE, 5867/24 ms [**A**], 4917/43 ms [**B**]). In PDw fast spin echo image [**A**], metal artifacts including spatial distortion and signal pile-up makes it difficult to evaluate the interface of the implant. The MAVRIC image [**B**] demonstrates more accuracy depiction of the implant, notably the tibial component, with clear visualization of the pegs. (*Courtesy of Dr. Corolyn Sofka, M.D., Associate Professor of Radiology, Weill Cornell Medical College, Hospital for special surgery, New York, NY*)

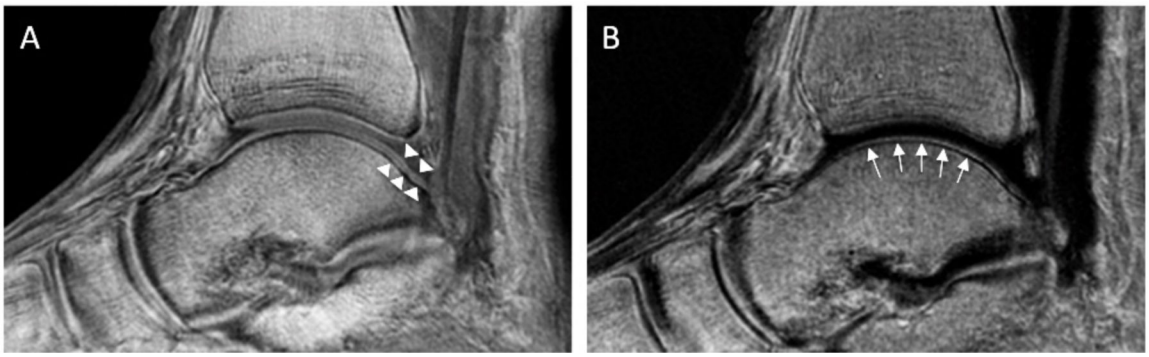

Fig. 8–.

Novel UTE MR imaging of the ankle joint.

A, Sagittal UTE image (TR/TE, 16/0.08 ms) demonstrated full thickness articular cartilage of the talar dome (arrow heads) with an intermediate signal intensity.

B, Echo subtraction image (TE 0.08 – TE 3.3 ms) demonstrated a thin curvilinear intermediate signal intensity of the calcified cartilage layer (arrows).

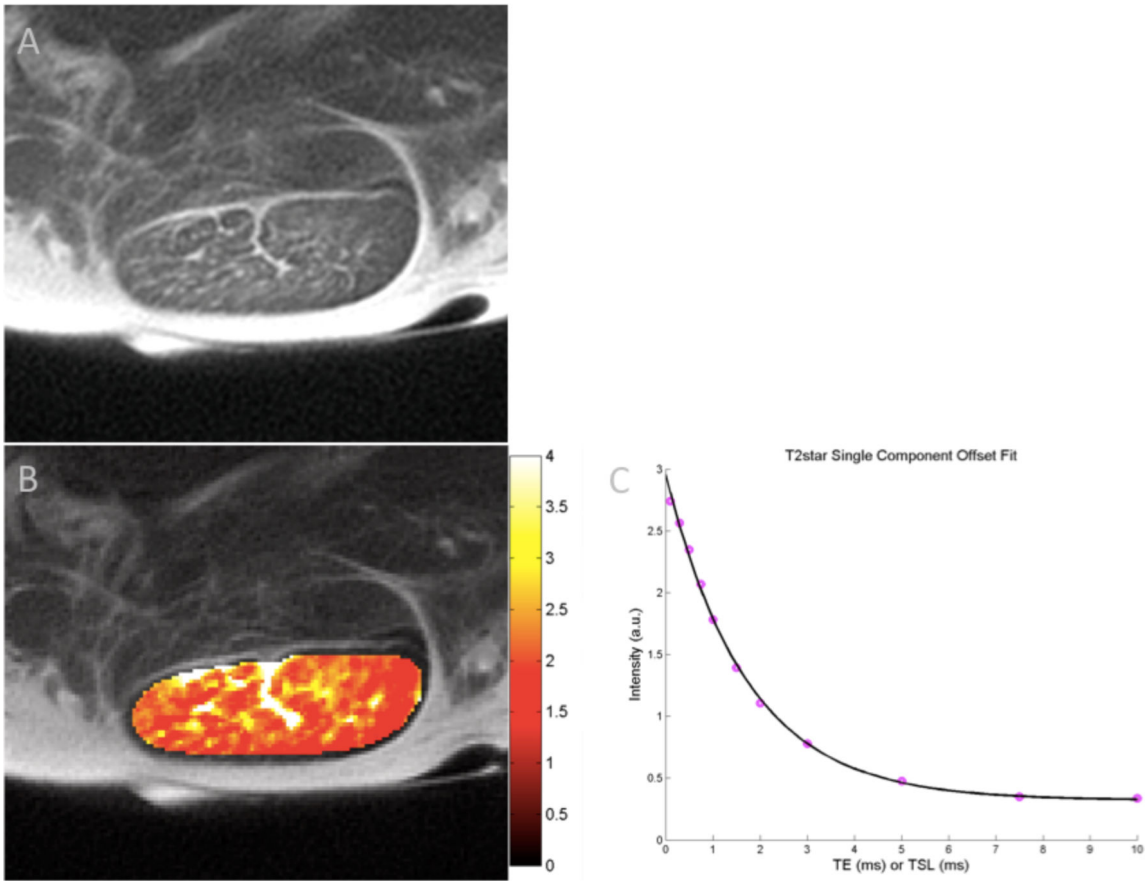

Fig. 9–.

Novel Ultrashort Time to Echo (UTE) MR imaging of the Achilles tendon.

A, Axial UTE image of the Achilles tendon (TR/TE, 400/0.1). Note intermediate signal intensity of the tendon that reveals internal fascicular pattern of the tendon fibers.

B, Color mapping of UTE T2* relaxation times (color range 0–4 ms).

C, Global region of interest UTE T2* quantification performed using single component fitting shows low noise and a T2* value of 1.7 milliseconds.

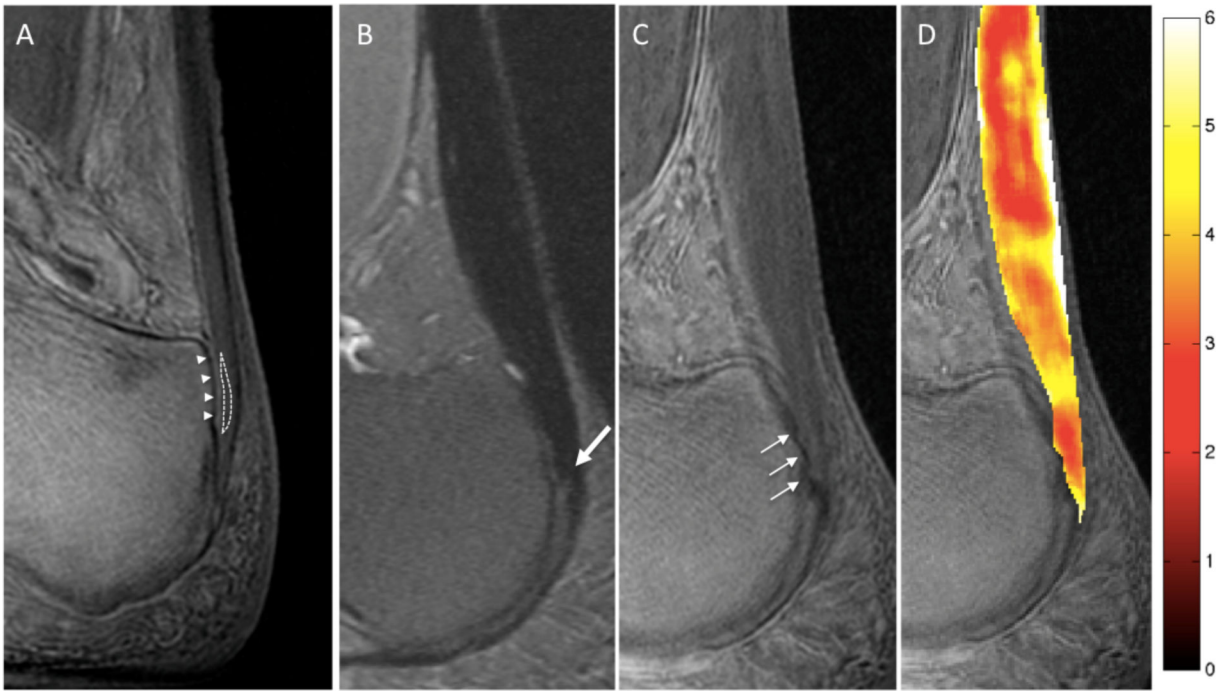

Fig. 10–.

Sagittal MR images of the calcaneus at Achilles tendon enthesis.

A, UTE MR image (TR/TE, 16/0.08 ms) in a 30 year old male without Achilles symptoms demonstrates fibrocartilaginous surface of the posterior calcaneus (arrow heads) and fibrocartilaginous nodules at inner Achilles tendon surface (dotted area).

B and **C**, proton density spin echo with fat saturation [**B**] and UTE [**C**] images of a 34 year old female presented with chronic posterior ankle pain (TR/TE, 3050/68 ms [**B**] and 16/0.08 ms [**C**]). Thickening and enlargement of the Achilles tendon was seen on the conventional image [**B**]. Small spurs (thick arrow) was noted at the attachment site. UTE image [**C**] demonstrated an absence of the fibrocartilage of posterior calcaneus (thin arrows) and Achilles surface suggestive of enthesopathy.

D, Colour mapping of UTE T2* relaxation time (color range 0–6 ms), diffuse heterogeneous prolong T2* relaxation time of the Achilles tendon is demonstrated.

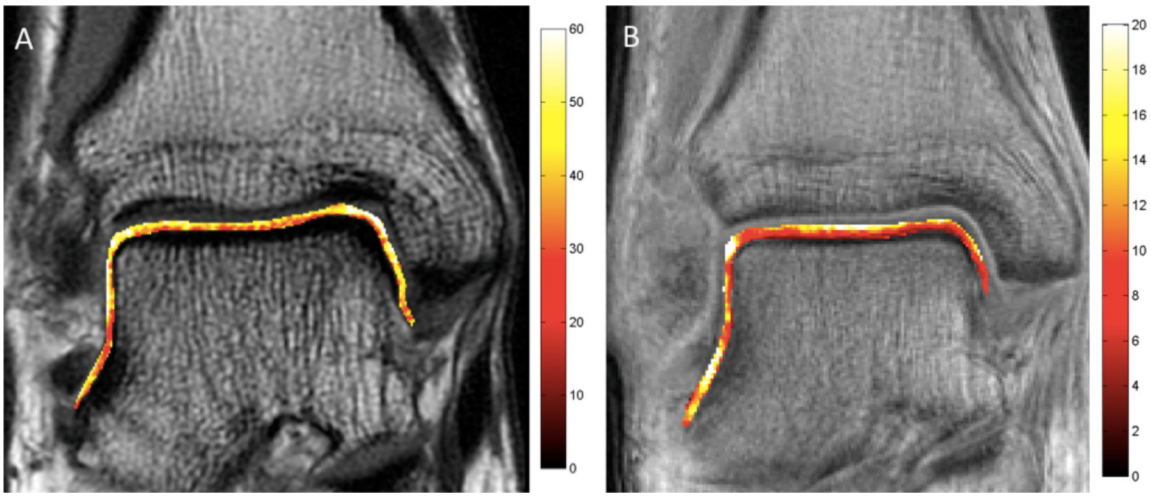

Fig. 11–.

A and B, Comparison of ankle MR image T2 mapping [**A**] and T2* mapping [**B**]. Coronal T2 mapping [**A**] (Variable TE, from 7.9 to 63.4 ms; Color range 0–60 ms) demonstrate diffuse homogeneous cartilage signal along articular surface. Coronal T2* mapping [**B**] (Variable TE from 0.08 to 5 ms; Color range 0–20 ms) demonstrate bilaminar pattern with lower T2* at inner calcified cartilage layer and higher T2* at more superficial cartilage layer.

TABLE 1:

Suggestion for routine ankle protocol on a 3.0 T scanner.

Plane and sequences without fat saturation	**TR/ TE (ms)**	**ST/space (mm)**	**FOV (cm)**	**Matrix**	**ETL**	**Scan Time (min:sec)** ***d***
Axial FSE PDw [a]	5000/33	3.3/0.5	11–15	512×256	12	2:25
Coronal FSE PDw [a]	5000/33	4/0.5	11–15	512×384	12	3:28
Sagittal FSE PDw [a]	4500/33	3/0.5	11–15	512×384	12	3:05
Plane and sequences with fat saturation						
Sagittal FSE-IR (IR170) [a]	4000/13	3.3/0.5	18	256×192	12	6:49
Axial FSE T2w FS [b]	3500/50	3.3/0.5	11–15	512×256	12	5:22
Coronal FSE T2w FS [b]	5000/45	4/0.5	11–15	512×384	12	5:25
Sagittal FSE T2w FS [c]	3500/50	3/0.5	11–15	512×384	12	7:42

Note

[a]Base protocol should include these sequences. T1-weighted sequence can replace FSE PDw in sagittal plane if desired, as the base protocol includes a fluid sensitive sagittal sequence with the FSE-IR.

[b]Possible additional sequences for evaluating ankle structures, with longer scan time as a trade off.

[c]Possible additional sequences that can use to replace Sagittal FSE-IR.

[d]Scan time was calculated on 3.0 T GE Discovery 750; GE Healthcare, Milwaukee, WI

Abbreviations: TR, repetitive time; TE, time to echo; SL, slice thickness; FOV, field of view; ETL, echo train length; FSE, fast spin echo; PDw, proton density-weighted; T2w, T2-weighted; FS, fat saturation; IR, inversion recovery.

TABLE 2:

Indication for protocol modification [a]

Considerate for additional plans	Recommended Sequence	Clinical conditions	Imaging conditions
Sagittal oblique peroneal plane [a]	FSE T2w or T2w with FS	• Tenderness of peroneal tendon • Crepitus on motion	• Inconclusive of peroneus tendon tear on routine protocol
Oblique tibiofibular syndesmosis plane [a]	FSE PDw or PDw with FS	• Anterior ankle pain after trauma •Positive external rotation stress maneuver	• Decrease overlapping of tibiofibular shadow in weight bearing x ray with subtle tear on routine protocol
Oblique calcaneofibular ligament plane [a]	FSE PDw with FS or T2w with FS	• High grade ankle sprain • Marked positive anterior drawer test • Positive Talar-tilt test	• Talar-tilt on x ray • Inconclusive of calcaneofibular ligament tear during routine protocol
IV Contrast administration	FSE T1W with subtraction or T1W with FS	• Suspicious of synovitis or tenosynovitis • Suspicious of tumor	• Subtle synovial proliferation on routine protocol • Indeterminate nature mass/nodule
Metal reduction sequences	FSE-IR, no chemical fat suppression FSE rather than SE Avoid gradient	• All cases with metal instrument with suspicious of parainstrumental lesion	• Metal instrument on radiograph or routine MR

Note−

[a]The additional planes should consider as problem solving sequences if **both** clinical and imaging conditions apply.

Abbreviations: FSE, fast spin echo; T2w, T2-weighted; FS, fat saturation; PDw, proton density-weighted.

TABLE 3:

Metal artifact reduction principle technique and availability.

Sequence	Availability	Technique	Principle	Result	Draw back
MARS	Most clinical magnets	Optimize conventional sequence	High-bandwidth sequences, increase section selection, increase echo train length, decrease echo spacing, and increase image matrix	Decrease in plane and geometric distortion Decrease signal loss by select spine-cho sequence	Through section distortion Low SNR
Advance WARP O MAR XD	Siemen Healthcare Phillip Healthcare	Multispectral technique SEMAC-VAT	Two-dimensional fast spine-echo or turbo spine-cho sequence with extending VAT and additional phase encoded in third dimension (Z-axis). Overlapping section gives a detailed map of how magnetic susceptibility has distorted the image. Then slice reconstruction by complex algorithm in order to shift them into proper position.	Further decrease in-plane and through-plane artifact	Relative long scan time May result in back folding artifact
MAVRIC	GE healthcare	Multispectral technique MAVRIC	Several three-dimensional standard spine-echo sequence that use difference off-resonance frequency-selective excitation that generate one combined data set.	Further decrease in-plane and through-plane artifact	Relative long scan time Require many phase encoding steps to cover entire region (questionable feasibility in large joint)
MAVRIC SL	GE healthcare	Multispectral technique	Hybrid sequence that combines z-phase encoding of SEMAC with variable resonance imaging combination of MAVRIC. Slice selection gradient is applied to each spectral bin and gradient is reapplied to achieve VAT	Even further decrease in-plane and through-plane artifact	Decrease spatial resolution contrast and less fat saturation in STIR

Abbreviations: MARS, metal artifact reduction sequence; SNR, signal to noise ratio; SEMAC, slice encoding for metal artifact correction; O MAR, orthopedic metal artifact reduction; VAT, view angle tilting; MAVRIC, multiacquisition with variable-resonance imaging combination.; STIR, short tau inversion recovery.

TABLE 4:

UTE MR imaging protocols.

Plane and sequences	TR (ms)	TE (ms)	Thickness/space (mm)	FOV (cm)	Matrix
Sagittal UTE ankle	15.6	0.08, 3.2, 6.4 and 9.6	2.5/0	12–14	384×384
Coronal UTE ankle	14.2	0.08, 3.2, 6.4 and 9.6	1.0/0	12–14	384×384
Axial UTE Achilles tendon	15.2	0.08, 3.2, 6.4 and 9.6	3.0/0	8–10	256×256